International Journal of Orthopaedics

Online Submissions: http: //www.ghrnet.org/index.php/ijo
doi: 10.17554/j.issn.2311-5106.2023.10.483

Int. J. of Orth. 2023 May 8; **10(1)**: 1721-1729
ISSN 2311-5106 (Print), ISSN 2313-1462 (Online)

ORIGINAL ARTICLE

Biomechanical Effects of Bone Quality and Implant Design on Femoral Damage Mechanism in Total Hip Arthroplasty

Aiman Izmin[1], Mitsugu Todo[1,2], Takuaki Yamamoto[3]

1 Interdisciplinary Graduate School of Engineering Sciences, Kyushu University, 6-1 Kasuga-koen, Kasuga, Fukuoka 816-8580, Japan;
2 Research Institute for Applied Mechanics, Kyushu University, 6-1 Kasuga-koen, Kasuga, Fukuoka 816-8580, Japan;
3 Department of Orthopedic Surgery, Faculty of Medicine, Fukuoka University, 7-45-1 Nanakuma, Jonan-ku, Fukuoka 814-0180, Japan.

Conflict-of-interest statement: The author(s) declare(s) that there is no conflict of interest regarding the publication of this paper.

Correspondence to: Mitsugu Todo, Interdisciplinary Graduate School of Engineering Sciences, Kyushu University, 6-1 Kasuga-koen, Kasuga, Fukuoka 816-8580, Japan.
Telephone: +81-92-583-7762
Email: todo@riam.kyushu-u.ac.jp

Received: March 13, 2023
Revised: April 6, 2023
Accepted: April 10 2023
Published online: May 8, 2023

ABSTRACT

Total hip arthroplasty (THA) has become a common solution to solve end-stage hip diseases of middle and old age patients. However, the complications following THA such as bone fracture might depend on the bone quality and implant design. A better outcome after THA could be achieved through the risk assessment from the early stage. Therefore, the aim of this study was to investigate the effects of bone quality and THA stem design on the mechanisms of micro-damage formation in femoral bones using CT-image based finite element method (CT-FEM). Two inhomogeneous bone models were developed from the CT images of 61 and 87-year-old patients and three types of stems were introduced to represent the corresponding THA models. Finite element analyses with a nonlinear damage analysis were then performed under the lateral bending and torsional conditions. It was observed that the implant geometries such as shoulder size, stem length, and cross-section shape influenced the damage behaviour of the models. The results suggested that the elderly patient had higher risk of implant loosening even at lower loading magnitude, compared to the younger patient. Several fracture locations were also predicted on both femoral models upon the complete failure. It was found that the fracture types can be clearly classified according to the Vancouver classification and the AO Foundation/Orthopaedic Trauma Association.

Key words: Total hip arthroplasty; Damage mechanism; Nonlinear finite element analysis; Bone quality; Implant design.

Izmin A, Todo M, Yamamoto T. Biomechanical Effects of Bone Quality and Implant Design on Femoral Damage Mechanism in Total Hip Arthroplasty. *International Journal of Orthopaedics* 2023; **10(1)**: 1721-1729 Available from: URL: http://www.ghrnet.org/index.php/ijo/article/view/3373

INTRODUCTION

Total hip arthroplasty (THA) is a common orthopaedics surgery performed as a solution to late-stage hip diseases such as osteoarthritis and femoral head necrosis. It is predicted that the total annual counts and utilization of THA will continue to grow globally in the following years, thus, the number of its complications may proportionally increase[1-3]. It has previously been reported that some of the common causes of revision surgeries following THA are mainly due to the loosening/osteolysis, dislocations, infections, and periprosthetic fractures[4]. Some of these causes are believed to have relations with bone quality, implant geometry and design[5,6].

In addition, the unique characteristic of bone with its irregular and inhomogeneous structure makes it more complex to understand the biomechanical related problems[7]. Different bones might produce different outcomes after the THA implantation, while different types of implant geometries might lead to other consequences. Due to this uncertainty, it is risky to simply apply one implant to every bone without any perception from the biomechanical point of view.

Recent years, CT-image based finite element method (CT-FEM) has been utilized to understand the biomechanical problems in the orthopaedical field[8-14]. Although the bone mineral density (BMD) has become the primary clinical parameter to assess the fracture risk of bones, recently it was found that an average value of BMD cannot be the single parameter which mainly controls the fracture risk in the case of vertebral compression fracture[13]. CT-FEM can convert the inhomogeneous distribution of BMD into the distribution of Young's modulus, hence able to predict the risk of bone fracture with high accuracy introducing the damage mechanics into the non-linear finite element analysis. This unique and effective computational method has been implemented in a field of bone biomechanics where the bone strength and fracture sites were successfully predicted[8-12,14-16], while in several classical computational biomechanical studies, the risk of bone fracture associated with THA was predicted through the evaluation of the stress and strain fields with the assumption of unrealistic homogeneous bone structures[17-19]. Meanwhile, studies with the use of cadavers could give us some realistic information of external fracture modes[20-22]; however it was impossible to perform the internal analysis and visualization.

The aim of this study was to characterize the effects of bone type and implant geometry on the mechanism of femoral fracture using CT-FEM. Two different three dimensional femoral models were constructed using the CT data obtained from two patients of age 61 and 87. Three different geometries of femoral stem were also selected and inserted into the femoral models to construct six different THA models. Then, the damage formations in the THA models were analysed using a non-linear finite element method with elemental damage models under two different boundary conditions, namely, lateral bending and torsion. The effects of bone type and stem geometry on the femoral fracture mechanism were then discussed on the basis of the computational results.

ANALYSIS METHOD

Construction of intact femoral models

Quantitative CT images of two female patients of 61 and 87-year-old were used to develop computational models. Both patients were diagnosed with stage three of avascular necrosis at the head of the right femur. Both CT images had a slice thickness of 0.5 mm. CT-FEM software, Mechanical Finder version 11.0 (Research Centre for Computational Mechanics Inc., Tokyo, Japan), was used to develop the three-dimensional FE models of the right femurs. Two-dimensional femoral bone region of interest (ROI) was selected from each slice of the CT images, where the bone region had higher CT values than that of the soft tissues such as muscle, ligament and adipose tissues. The selected ROI at each CT image was vertically stacked to finally form the three-dimensional geometry of the femur. Next, the FE model of the intact femur was meshed with 2-mm tetrahedral elements for the cancellous bone and inner cortical bone, whereas 2-mm triangular shell elements with a thickness of 0.3 mm were assigned to the outer surface of the cortical bone. The surface shell elements were assigned to express the stiffest layer of the cortical bone that cannot be expressed from the CT images[15]. The FE models of the 61 and 87-year-old patient were thereafter denoted with bone X and Y, respectively. The numbers of solid and shell elements of the intact model of bone X and Y were 156509, 191478, and 73698, 84954, respectively. The inhomogeneous BMD values were introduced into every element by converting the Hounsfield unit (HU) into BMD using a linear formula[15].

Construction of THA models

Three different types of femoral stem were introduced in this study and denoted by stem I, stem II, and stem III. Each stem came with a different design and geometry as illustrated in Figure 1. In reconstructing the virtual hip arthroplasty, the femoral bone head was osteotomized based on the intertrochanteric line to approximately 1 cm above the lesser trochanter. The osteotomy of the femoral head was performed by considering the stem geometry, i.e., the medial offset, vertical height, and neck length. The stem was then properly aligned into the femoral canal by referring to the mapping view from the CT images. The THA models of bone X and Y implanted with stem I, II, and III are shown in Figure 2. The FE models of bone X implanted with stem I, II and III were constructed with 162,710, 155,220, 139,579 of tetrahedron solid elements and 62,628, 61,533, 62,547 of triangular shell elements, respectively. For bone Y, 189,777, 185,391, 175,221 of solid elements and 74,766, 74,190, 75,165 of shell elements were used with stem I, II, and III. The materials of the stem and femoral ball were assumed to be Titanium alloy and Alumina ceramic, respectively. It is noted that the interface between the bone and stem was assumed to be perfectly bonded.

2.3. Boundary conditions

Two different boundary conditions were introduced into the nonlinear FE analysis in order to predict the damage formations of the two types of femoral bone. These conditions were implemented on the basis of the validated and well-established testing protocol for periprosthetic femoral shaft fixation[23-27]. In the boundary conditions,

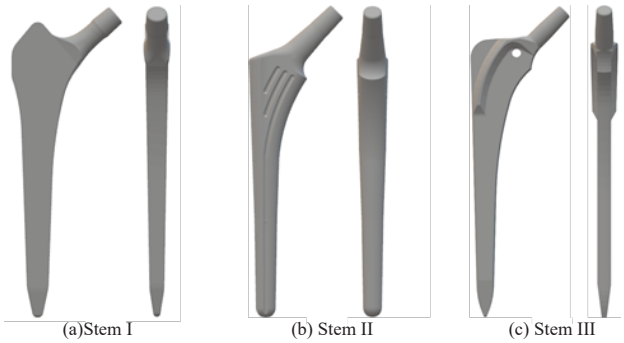

(a)Stem I (b) Stem II (c) Stem III

Figure 1 Illustrations of three stem models.

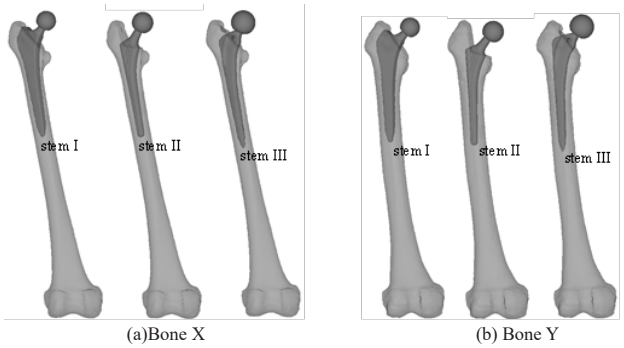

(a)Bone X (b) Bone Y

Figure 2 THA models constructed by combining a femoral model and a stem

two different types of isometric loadings were introduced and they were thereafter denoted as lateral bending condition (LBC) and torsional condition (TC). The loading direction was set based on the angle of α and β, which represent the long axis of the femur in the frontal and sagittal plane, respectively. The orientation of loading direction for LBC was α = 90°, β = 0°, and for TC, α = 90°, β = 90°. The boundary conditions, LBC and TC, are shown in Figure 3. For both LBC and TC, the magnitude of applied load was set to be increased stepwise, ranging from 0 N to 1500 N in 20 steps (75 N per step). The selected range of loading magnitude was found to be sufficient to demonstrate the damage mechanisms in femoral fracture under the same conditions in the previous study[14].

Mechanical theories and material properties

The tensile deformation of all the elements constructing the femoral models was assumed to be expressed by the linear elastic response, in which the stress-strain relation was characterized by two material constants such as Young's modulus and Poisson's ratio. On the contrary, the compressive deformation of the elements was assumed to be expressed by the bi-linear elastic-plastic response, in which the stress-strain relation was characterized by Young's modulus and Poisson's ratio under the linear-elastic behavior and the yield stress and the work hardening coefficient under the plastic behavior. The Drucker-Prager yield condition was used to assess the onset of yielding[15]. Yielding was assumed to take place when the Drucker-Prager equivalent stress reached the compressive yield stress. Young's modulus and the compressive yield stress of a solid element were calculated from the corresponding BMD value of the element using the empirical formulae proposed by Keyak et al[28] and Keller[29] as shown in Table 1. Poisson's ratio and the work hardening coefficient of all the solid elements were set to 0.4 and 0.05, respectively. Those properties of each of the shell elements were chosen so that they were equivalent to those of the adjacent solid element located under its position.

The tensile fracture of a solid or a shell element was assumed to take place when the maximum principal stress reached the tensile strength which was equal to 0.8 times the compressive yield stress of the element[30,31]. On the other hand, the compressive fracture of the element was assumed to occur when the minimum principal strain reached the fracture strain which was equal to -3,000 micro-strain[31,32].

Table 1 Relationship between bone mineral density and the material properties [26,27]

Bone mineral density (g/cm^3)	Young's modulus (E)
= 0	0.001
0 < ≤ 0.27	33,900
0.27 < ≤ 0.6	5307
0.6 <	10,200
Bone mineral density (g/cm3)	Yield stress (MPa)
< 0.317	137
0.317 ≤	114

Table 2 Failure criterions under tensile and compressive stress states.

Stress state		Criterion
Tension	Initiation of failure	$\sigma p = 0.8\sigma y$
Compression	Transition to yielded state	$\sigma D = \sigma y$
	Initiation of failure	$\varepsilon p = -3000$

σp = maximum principal stress; σy = yield stress under compression; σD = Drucker-Prager equivalent stress; εp = minimum principal strain.

Those criterions are summarized in Table 2. Aggregation of shell element failures is usually needed to express the femoral fracture of the outer cortical surface and compare the fracture behaviour between the intact and the THA models. Therefore, in this study, a critical condition was set on the basis of the number of failure elements. 1000

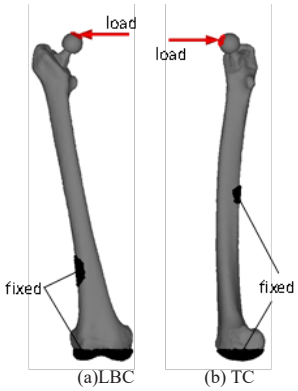

Figure 3 Boundary conditions.

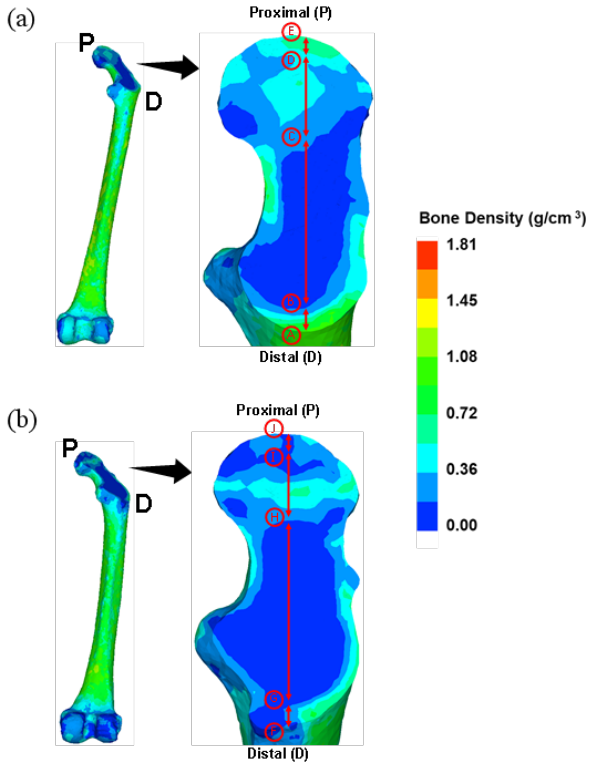

Figure 4 Inhomogeneous distribution of bone mineral density: (a) bone X and (b) bone Y.

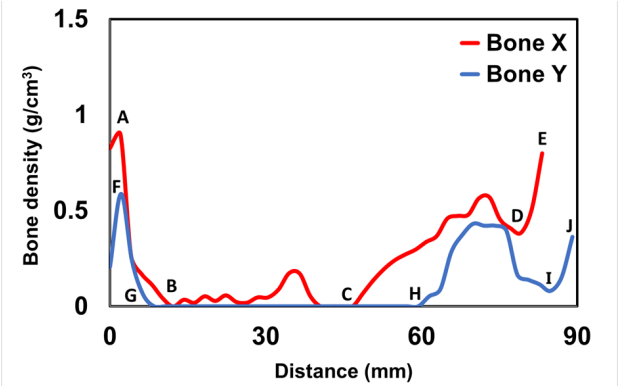

Figure 5 Comparison of BMD distribution of bone X and bone Y.

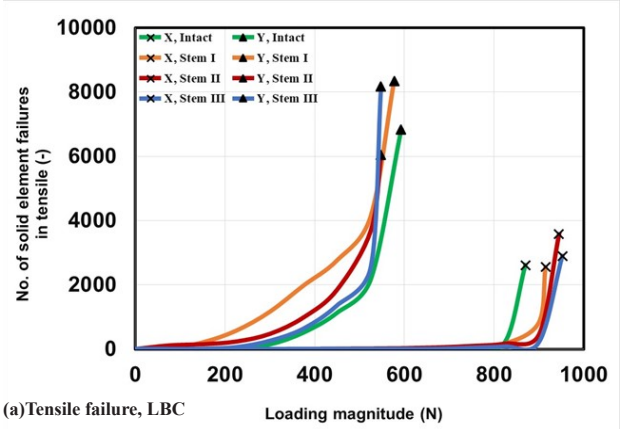

(a)Tensile failure, LBC

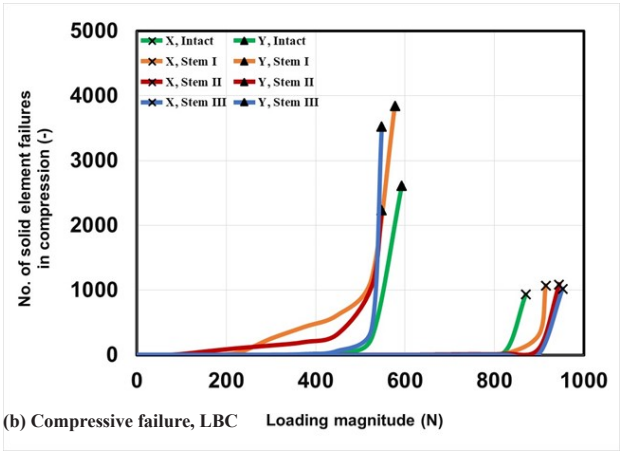

(b) Compressive failure, LBC

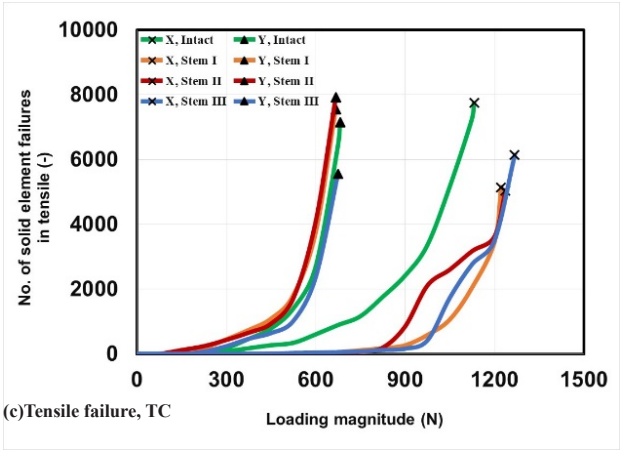

(c)Tensile failure, TC

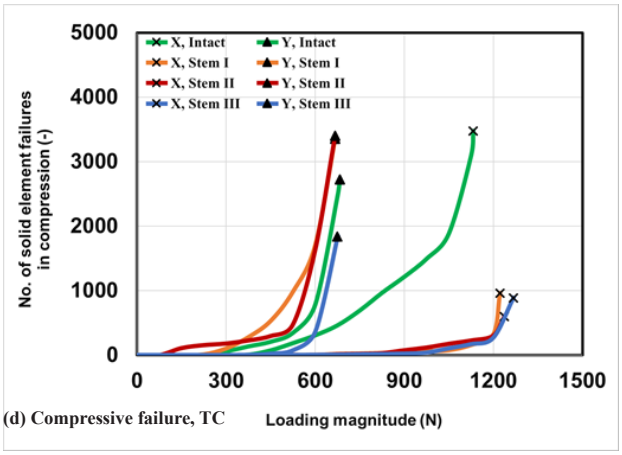

(d) Compressive failure, TC

Figure 6 Cumulative number of solid element failures under LBC and TC.

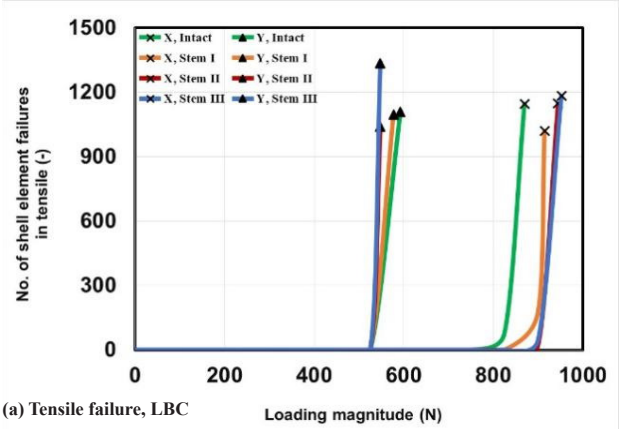

(a) Tensile failure, LBC

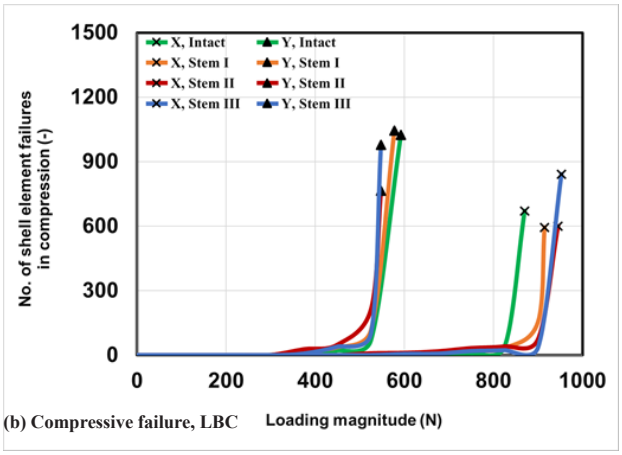

(b) Compressive failure, LBC

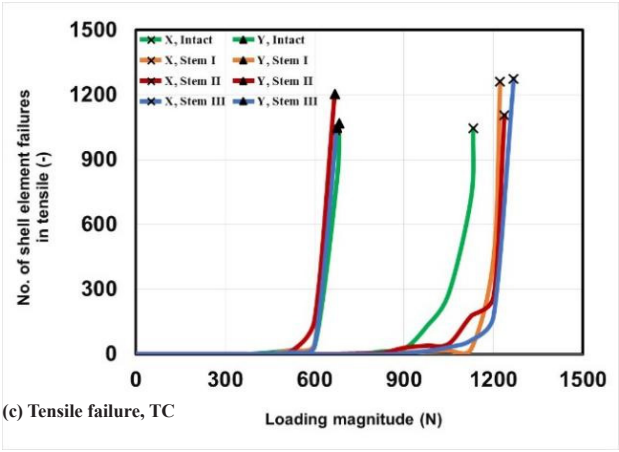

(c) Tensile failure, TC

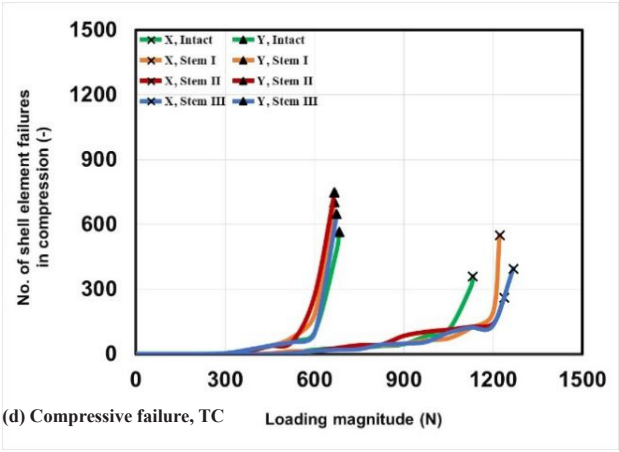

(d) Compressive failure, TC

Figure 7 Cumulative number of shell failures under LBC and TC.

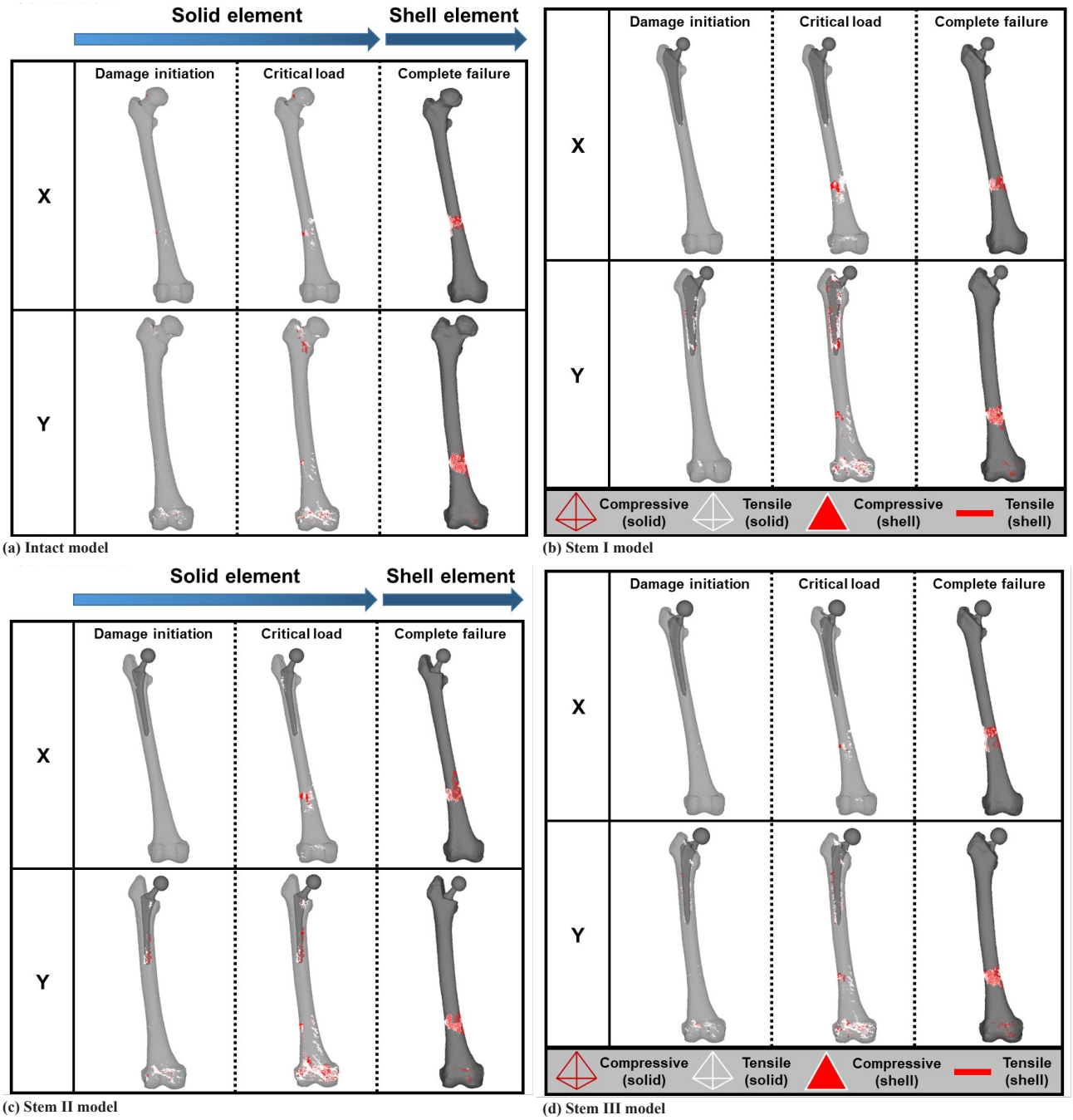

Figure 8 Distributions of solid and shell element failures under LBC.

shell element failures were chosen as the condition and the analyses were terminated when the total number of shell element failures reached 1000 under either tensile stress or compressive stress state.

The stress-strain responses of titanium alloy and alumina ceramic were assumed to be linear elastic. Young's modulus and Poisson's ratio were chosen to be 114 GPa and 0.34 for titanium alloy and 370 GPa and 0.22 for alumina ceramic[33].

RESULTS AND DISCUSSION

Distribution of bone mineral density

Figures 4(a) and (b) illustrate the inhomogeneous distribution of BMD in bone X and bone Y, respectively. The head and neck areas of the femurs were vertically cut to have the cross-sectional views of the areas. For each bone model, the extraction points were selected at every threshold of the contours along the line from distal (D) to proximal (P), and the average BMD values were extracted. The BMD distributions along the lines are shown in Figure 5. Point A to B and F to G indicate the distal cortical bone area of bone X and bone Y, respectively. Point B to C and G to H correspond to the areas of bone marrow, C to D and H to I are the areas of cancellous bone, while D to E and I to J are the areas of cortical bone at the proximal femur for both bones, respectively. It was found that BMD values of bone X were greater than bone Y in every bone segment, e.g., cortical and cancellous bone throughout the distance. A notable difference of BMD was observed in the distal cortical, cancellous, and proximal cortical bone, i.e., 0.31 g/cm^3, 0.13 g/cm^3, and 0.43 g/cm^3, respectively. Obviously aging was thought to be the key factor of this finding, where the increased porosity of the elder bone reduced its density and mass[34].

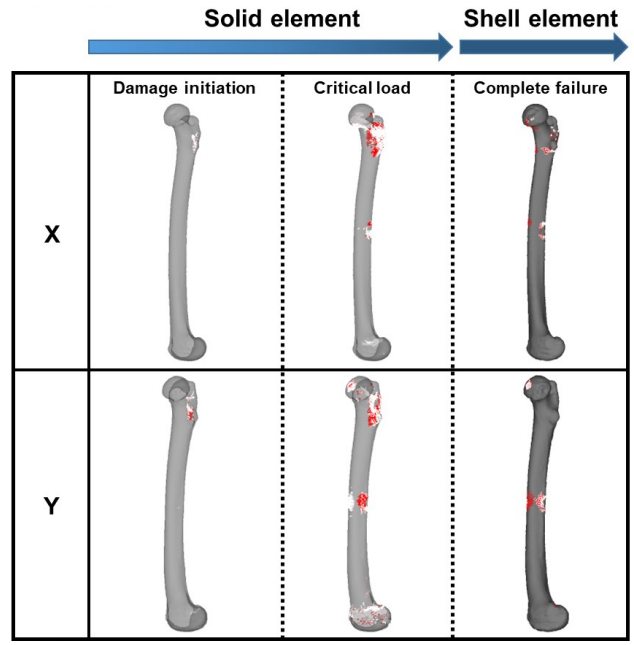

(a) Intact model

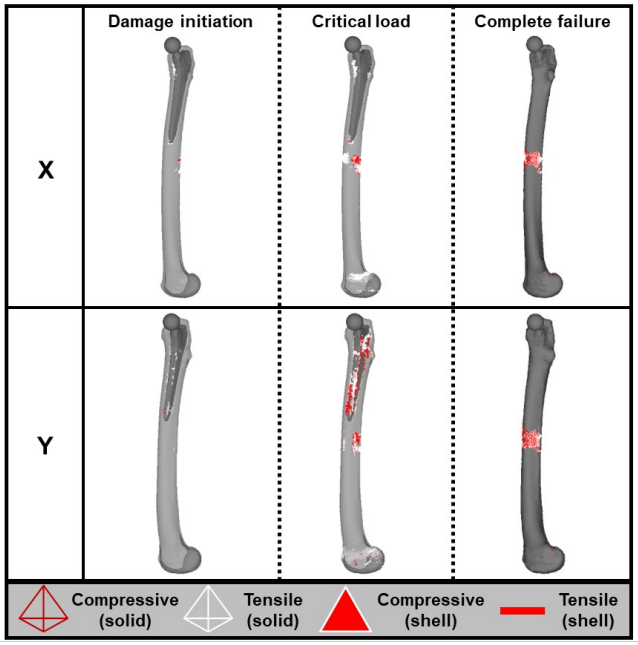

(b) Stem I model

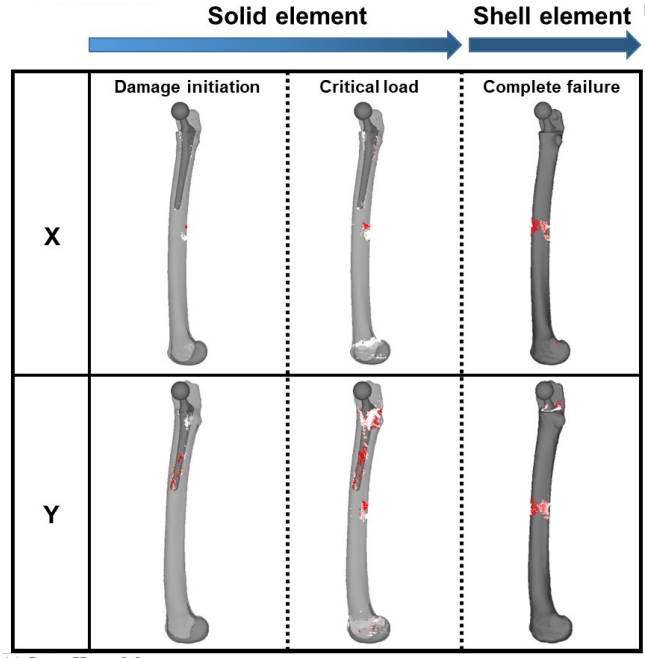

(c) Stem II model

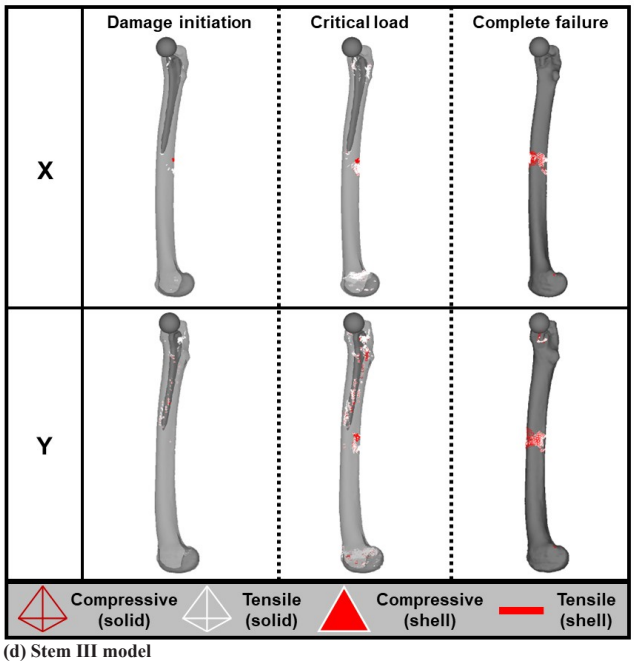

(d) Stem III model

Figure 9 Distribution of solid and shell element failures under TC.

Accumulation of element failures as bone micro-damage

Figure 6 shows the cumulative numbers of solid element failures under LBC and TC. Figures (a) and (c) and Figures (b) and (d) correspond to the element failures generated under tensile and compressive conditions, respectively. It can be seen that the solid element failures under the tensile stress state were dominant compared to the compressive state for both LBC and TC. The cumulative numbers tended to gradually increase up to the final load level, and rapidly increase at the final load under both LBC and TC. It should be noted that the final levels of load of bone X models were much higher than those of bone Y models, suggesting that the strength of bone X at the final bone fracture was much greater than that of bone Y. It is important to see that in bone Y, the stem insertion tended to lower the bone strength, while in bone X, the bone strength tended to increase due to the stem insertion. Under both LBC and TC, the effects of stem design on the element failure behaviour and final load level were found to be very small.

The cumulative numbers of shell element failures under LBC and TC are also shown in Figure 7. Similar to the solid element failures, the tensile failures tended to be more dominant than the compressive failures. Under LBC, for both bone X and bone Y, the numbers of shell element failures under tension and compression rapidly increased at the final stage of loading. Thus, the element failures were led by the solid elements and then finally the shell element failures took place. It is also clearly seen that bone X is much stronger than bone Y for both intact and stem insertion models.

Distribution of solid and shell element failures

Distribution patterns of element failures as bone micro-damages are

shown in Figures 8 and 9 for LBC and TC, respectively. In those images, distributions of solid element failures at the damage initiation and the critical load stages, corresponding to the final bone fracture, are presented, along with the distributions of shell element failures at the final bone fracture (called 'complete failure'). It is clearly seen that bone Y had greater internal bone damages than bone X in both damage initiation and critical load stages. In the intact models, solid element failures mainly generated in the femoral neck region and the distal side close to the knee joint under LBC. On the other hand, solid element failures generated in the femoral neck and the middle region of diaphysis under TC. It is worth noting that the distal side and the middle region corresponded to the fixed regions set as the boundary conditions under LBC and TC, respectively. Also, shell element failures at the complete failure mainly generated in those regions.

When a stiffer metallic stem was inserted into the femoral bone, it subsequently changes the mechanical environment of the bone. From the figures, the presence of stem easily damaged the cancellous bones that surrounded the stem in bone Y compared to bone X, where quite noticeable damage was seen even in the lower loading magnitude as illustrated in the damage initiation stage. Such severe bone damage that appeared along the bone-stem interface of bone Y may affect the primary stability of the implant after the arthroplasty. Without primary stability, the process of osseointegration may probably be delayed. In addition, the high number of failure elements at the bone-stem interface may contribute to the risk of implant loosening due to the failure of the cancellous bones surrounding the stem. This phenomenon may also contribute to the risk of periprosthetic fracture after THA where loosening of the stem was known as one of the risk factors[35-39].

The effect of stem geometry and design on the internal bone damage, i.e. solid element failures, can be seen in bone X under TC. Based on Figure 6(c), each stem exhibited different behaviour of solid element failures which occurred between the load 900 N and 1200 N. Bone X with Stem II initially experienced the increasing trend, followed by Stem III and Stem I. This behaviour might be related to the different design of stem shoulder. Stem I has the widest shoulder width with a rectangular cross-section, while stem III also has a rectangular cross-section with smaller shoulder width. The shoulder width of stem II is comparable to stem III, however, with a circular cross-sectional shape. Differences in the shoulder size and the cross-sectional shape of the stem might affect the formation of internal bone damage. From the observation, smaller shoulder sizes tend to have early increments of bone damage compared to the stem with wider shoulders. A wider shoulder with a rectangular cross-sectional shape could produce a much higher torsional resistance when the implant is surrounded by cancellous bones with higher strength.

Solid element failures within the bone-stem interface at the critical stage

The numbers of solid element failures within the bone-stem interface at the critical stage are shown in Figure 10. A similar extraction size of 70 mm × 70 mm × 180 mm was applied to all models that enclosed the area of the bone and the stem. It is clearly seen that the number of element failures of bone X was much lower than that of bone Y for all stem types. From this finding, it is understood that bone with poor quality will experience greater internal bone damage specifically at the interfacial area of bone and stem. The small number of element failures suggests that bone X may have greater primary stability with stem, allowing the osseointegration process to occur. For bone Y, the highest number of element failures was obtained at stem I model. From this result, it can be said that the stem with larger dimensions

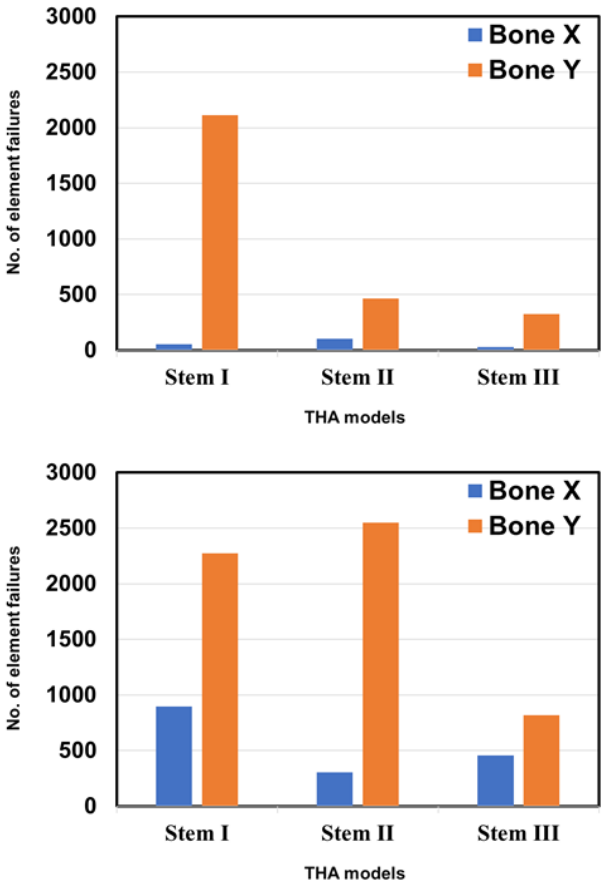

Figure 10 (a) LBC and (b) TC.

may produce major damage to the cancellous bones. The bones with low strength due to lower BMD may easily be damaged when they are in contact with stiffer material, hence resulting in the significant number of element failures in stem I model compared to stem II and III models.

It is understood from Figure (b) that bone X with stem I had the highest number of element failures at the critical stage under TC. This was similar to the bone Y with Stem I under LBC condition. In the case of bone Y, however, Stem I and Stem II shared almost similar numbers of element failures. The lowest number of element failures was obtained by Stem III. This phenomenon might be related to the factor of stem length. In this study, both loading configurations of LBC and TC will lead the bone to experience the bending process, thus, the factor of longer stem length will affect the bending behaviour of the bone.

Classification of femoral fractures following total hip arthroplasty

The assessment of the femoral bone fractures was based on the resulting failure of shell elements in the THA models. The fracture classification of the bone following THA was based on the Vancouver Classification and the AO Foundation/Orthopaedic Trauma Association (AO/OTA)[40,41]. In the case of LBC, the fracture of bone X was located only at the distal diaphyseal segment of the femur, while for bone Y, two locations were identified, i.e., distal diaphyseal and distal end segment of the femur as shown in Figure 8 (b)-(d), complete failure of shell element. The fracture located at the distal diaphyseal segment drew a parallel view to the Vancouver

classification type C. An oblique fracture pattern was observed in both bones. In regard to the fracture located at the distal end segment of bone Y, the view is almost similar to type 33-A-2.3, extra-articular, simple fracture with a transverse pattern from the AO/OTA classification. This fracture type was observed to occur at all of the THA models of bone Y.

Shell element failures of Figure 9 (b)-(d) illustrate the prediction of bone fracture under TC. The THA models of bone X fractured only at the middle diaphyseal segment, while two locations were observed for the THA models of bone Y, namely, the middle diaphyseal and trochanteric region. The fracture predicted at the middle diaphyseal segment was correlated to the type B_2 in the Vancouver classification. It is observed that the THA models of bone X had a spiral fracture pattern, while the THA models of bone Y were similar to the transverse pattern. On the other hand, quite noticeable fractures were seen at the trochanteric regions of bone Y implanted with Stem II and III, which suggests the possibility of Vancouver classification type A_G.

CONCLUSIONS

CT-FEM was utilized to predict the damage mechanism between two bones with different quality implanted with three types of THA stem. The bone quality was successfully assessed through the comparison of BMD distribution. It was found that the manipulating parameters such as bone quality and implant design influenced the micro-damage behaviours of the intact bone and THA models. In addition, the internal failures were mainly correlated to the implant geometry, while the external failures were associated with the boundary conditions. The damage mechanisms in both internal and external regions could further explain the biomechanical problems such as the risk of implant loosening and bone fracture. It is concluded that CT-FEM can be a useful tool to elucidate the mechanical problems associated with THA and improve the THA design and therefore, develop advanced implant designs.

REFERENCES

1 H. Katano, N. Ozeki, Y. Kohno, Y. Nakagawa, H. Koga, T. Watanabe, T. Jinno, and I. Sekiya, "Trends in arthroplasty in Japan by a complete survey, 2014-2017," *J Orthop Sci.* 2021 Sep; 26(5): *812-822*, [PMID: 32933832]; [DOI: 10.1016/j.jos.2020.07.022]

2 S. Kurtz, K. Ong, E. Lau, F. Mowat, and M. Halpern, "Projections of primary and revision hip and knee arthroplasty in the United States from 2005 to 2030," *J. Bone Jt. Surg.* 2007 Apr; 89(4): 780-5. [PMID: 17403800]; [DOI: 10.2106/JBJS.F.00222]

3 C. Pabinger, H. Lothaller, N. Portner, and A. Geissler, "Projections of hip arthroplasty in OECD countries up to 2050," *HIP Int.*, 2018 Sep; 28(5): 498-506. [PMID: 29783896]; [DOI: 10.1177/1120700018757940]

4 Z. K. Wszolek and R. F. Pfeiffer, *Swedish Arthroplasty Register Annual report 2014.*, vol. 21, no. 5. 2015.

5 A. V. Carli, J. J. Negus, and F. S. Haddad, "Hip arthroplasty: Avoiding and managing problems periprosthetic femoral fractures and trying to avoid them what is the contribution of femoral component design to the increased risk of periprosthetic femoral fracture?," *Bone Jt. J.*, 2017 Jan; 99-B(1 Supple A): 50-59. [PMID: 28042119]; [DOI: 10.1302/0301-620X.99B1.BJJ-2016-0220.R1]

6 S. W. Lee, W. Y. Kim, J. H. Song, J. H. Kim, and H. H. Lee, "Factors affecting periprosthetic bone loss after hip arthroplasty," *Hip Pelvis*, 2021 Jun; 33(2): 53-61. [PMID: 34141691]; [PMCID: PMC8190495]; [DOI: 10.5371/hp.2021.33.2.53]

7 M. Moazen, A. C. Jones, Z. Jin, R. K. Wilcox, and E. Tsiridis, "Periprosthetic fracture fixation of the femur following total hip arthroplasty: A review of biomechanical testing," *Clin. Biomech.*, 2011 Jan; 26(1): 13-22. [PMID: 20888674]; [DOI: 10.1016/j.clinbiomech.2010.09.002]

8 M. Todo, "Biomechanical Analysis of Hip Joint Arthroplasties using CT-Image Based Finite Element Method," *J. Surg. Res.*, 2018; 1(2): 34-41. [DOI: 10.26502/jsr.1002005].

9 M. Todo and K. Fukuoka, "Biomechanical Analysis of Femur with THA and RHA implants using CT-Image Based Finite Element Method," *J. Orthop. Sport. Med.*, 2020; 2(2): 89-107. [DOI: 10.26502/josm.511500024].

10 A. H. Abdullah and M. Todo, "Effects of Hip Arthroplasties on Bone Adaptation in Lower Limbs: A Computational Study," *J. Biosci. Med.*, 2015; 3(4): 1-7. [DOI: 10.4236/jbm.2015.34001].

11 A. H. Abdullah and M. Todo, "Stress Evaluation of Lower Limbs with Hip Osteoarthritis and Hip Arthroplasty," *J. Med. Bioeng.*, 2015; 4(2): 100-104. [DOI: 10.12720/jomb.4.2.100-104].

12 A. H. Abdullah, M. Todo, Y. Nakashima, and Y. Iwamoto, "Risk of Femoral Bone Fractures in Hip Arthroplasties during Sideway Falls," *Int. J. Appl. Phys. Math.*, 2014; 4(4): 286-289. [DOI: 10.7763/ijapm.2014.v4.300].

13 S. Wu, M. Todo, D. Umebayashi, and Y. Yamamoto, "Risk assessment of vertebral compressive fracture using bone mass index and strength predicted by computed tomography image based finite element analysis," *Clin. Biomech.*,2021 May; 85: 105365. [PMID: 33964689]; [DOI: 10.1016/j.clinbiomech.2021.105365]

14 A. H. Abdullah, M. Todo, and Y. Nakashima, "Prediction of damage formation in hip arthroplasties by finite element analysis using computed tomography images," *Med. Eng. Phys.*, 2017 Jun; 44: 8-15. [PMID: 28373012]; [DOI: 10.1016/j.medengphy.2017.03.006]

15 M. Bessho, I. Ohnishi, J. Matsuyama, T. Matsumoto, K. Imai, and K. Nakamura, "Prediction of strength and strain of the proximal femur by a CT-based finite element method," *J. Biomech.*, 2007; 40(8): 1745-53. [PMID: 17034798]; [DOI: 10.1016/j.jbiomech.2006.08.003].

16 M. Bessho, I. Ohnishi, T. Matsumoto, S. Ohashi, J. Matsuyama, K. Tobita, M. Kaneko, and K. Nakamura, "Prediction of proximal femur strength using a CT-based nonlinear finite element method: Differences in predicted fracture load and site with changing load and boundary conditions," *Bone*, 2009 Aug; 45(2): 226-31. [PMID: 19398043]; [DOI: 10.1016/j.bone.2009.04.241]

17 N. F. Ismail, S. Shuib, M. A. Yahaya, A. Z. Romli, and A. A. Shokri, "Finite element analysis of uncemented total hip replacement: The effect of bone-implant interface," *Int. J. Eng. Technol.*, 2018; 7(4): 230-234. [DOI: 10.14419/ijet.v7i4.26.22173].

18 D. K. Kwak, S. H. Bang, S. J. Lee, J. H. Park, and J. H. Yoo, "Effect of stem position and length on bone-stem constructs after cementless hip arthroplasty," *Bone Jt. Res.*, 2021 Apr; 10(4): 250-258. [PMID: 33820433]; [PMCID: PMC8076980]; [DOI: 10.1302/2046-3758.104.BJR-2020-0043.R3]

19 M. S. Yusof, N. Aznan, N. Fazli, A. Manan, S. H. Marwan, M. H. Mazlan, and A. H. Abdullah, "Effects of Varus and Sagittal Implant Positioning to the Stress Adaptation in Cementless Hip Arthroplasty," *Malaysian J. Med. Heal. Sci.*, vol. 17(SUPP13), no. 5, pp. 22-27, 2021.

20 J. N. Lamb, J. Baetz, B. H. Van Duren, A. Redmond, R. M. West, M. M. Morlock, and H. G. Pandit, "A calcar collar is protective against early periprosthetic femoral fracture around cementless femoral components in primary total hip arthroplasty A," pp. 779-786. [DOI: 10.1302/0301-620X].

21 E. Schwarz, G. Reinisch, A. Brandauer, S. Aharinejad, W. Scharf, and K. Trieb, "Load transfer and periprosthetic fractures after total hip arthoplasty: Comparison of periprosthetic fractures of femora implanted with cementless distal-load or proximal-load femoral components and measurement of the femoral strain at the time

of implant," *Clin. Biomech.*, vol. 54, no. July 2017, pp. 137-142, 2018 [DOI: 10.1016/j.clinbiomech.2018.03.010].

22 D. Delimar, "Impact Of Cementless Zweymuller Stem Anteversion On Resistance To Periprosthetic Fracture In Total Hip Arthroplasty," Acta Clin Croat. 2022 Feb; 60(3): 429-434. [PMID: 35282477]; [PMCID: PMC8907947]; [DOI: 10.20471/acc.2021.60.03.13]

23 M. G. Dennis, J. A. Simon, F. J. Kummer, K. J. Koval, and P. E. Di Cesare, "Fixation of periprosthetic femoral shaft fractures: A biomechanical comparison of two techniques," *J. Orthop. Trauma*, 2001 Mar-Apr; 15(3): 177-80. [PMID: 11265007]; [DOI: 10.1097/00005131-200103000-00005]

24 E. Fulkerson, K. Koval, C. F. Preston, K. Iesaka, F. J. Kummer, and K. A. Egol, "Fixation of Periprosthetic Femoral Shaft Fractures Associated With Cemented Femoral Stems," *J. Orthop. Trauma*, 2006 Feb; 20(2): 89-93. [PMID: 16462560]; [DOI: 10.1097/01.bot.0000199119.38359.96]

25 M. Talbot, R. Zdero, and E. H. Schemitsch, "Cyclic loading of periprosthetic fracture fixation constructs," *J. Trauma - Inj. Infect. Crit. Care*, 2008 May; 64(5): 1308-12. [PMID: 18469655]; [DOI: 10.1097/TA.0b013e31811ea244]

26 R. Zdero, R. Walker, J. P. Waddell, and E. H. Schemitsch, "Biomechanical evaluation of periprosthetic femoral fracture fixation," *J Bone Joint Surg Am.* 2008 May; 90(5): 1068-77. [PMID: 18451400]; [DOI: 10.2106/JBJS.F.01561]

27 J. K. Choi, T. R. Gardner, E. Yoon, T. A. Morrison, W. B. Macaulay, and J. A. Geller, "The effect of fixation technique on the stiffness of comminuted vancouver B1 periprosthetic femur fractures," *J. Arthroplasty*, 2010 Sep; 25(6 Suppl): 124-8. [PMID: 20558031]; [DOI: 10.1016/j.arth.2010.04.009]

28 J. H. Keyak, S. A. Rossi, K. A. Jones, and H. B. Skinner, "Prediction of femoral fracture load using automated finite element modeling," *J. Biomech.*, 1998 Feb; 31(2): 125-33. [PMID: 9593205]; [DOI: 10.1016/s0021-9290(97)00123-1

29 T. S. Keller, "Predicting the compressive mechanical behavior of bone," *J. Biomech.*, 1994 Sep; 27(9): 1159-68. [PMID: 7929465]; [DOI: 10.1016/0021-9290(94)90056-6]

30 T. M. Keaveny, E. F. Wachtel, W. C. Hayes, and C. A. Dana, "Journal of Biomechanics Volume 27 issue 9 1994 [doi 10.1016_0021-9290(94)90054-x] Tony M. Keaveny; Edward F. Wachtel; Catherine M. Ford; Wilson C. -- Differences between the tensile and compress_2.pdf," vol. 27, no. 9, 1994.

31 T. S. Kaneko, M. R. Pejcic, J. Tehranzadeh, and J. H. Keyak, "Relationships between material properties and CT scan data of cortical bone with and without metastatic lesions," *Med Eng Phys.* 2003 Jul; 25(6): 445-54. [PMID: 12787982]; [DOI: 10.1016/s1350-4533(03)00030-4]

32 L. Røhl, E. Larsen, F. Linde, A. Odgaard, and J. Jørgensen, "Tensile and compressive properties of cancellous bone," *J. Biomech.*, 1991; 24(12): 1143-9. [PMID: 1769979]; [DOI: 10.1016/0021-9290(91)90006-9]

33 M. I. Z. Ridzwan, S. Shuib, A. Y. Hassan, A. A. Shokri, and M. N. Mohammad Ibrahim, "Problem of stress shielding and improvement to the hip implant designs: A review," *J. Med. Sci.*, 2007; 7(3): 460-467. [DOI: 10.3923/jms.2007.460.467].

34 X. Wang, X. Shen, X. Li, and C. Mauli Agrawal, "Age-related changes in the collagen network and toughness of bone," *Bone*, 2002 Jul; 31(1): 1-7. [PMID: 12110404]; [DOI: 10.1016/s8756-3282(01)00697-4]

35 J. S. Bethea, J. R. DeAndrade, L. L. Fleming, S. D. Lindenbaum, and R. B. Welch, "Proximal femoral fractures following total hip arthroplasty," *Clin. Orthop. Relat. Res.*, 1982; 170: 95-106,. DOI: 10.1097/00003086-198210000-00013].

36 H. O. Fredin, H. Lindberg, and A. S. Carlsson, "Femoral fracture following hip arthroplasty," *Acta Orthop.*, 1987 Feb; 58(1): 20-2. [PMID: 3577736]; [DOI: 10.3109/17453678709146336]

37 J. S. Jensen, G. Barfod, D. Hansen, E. Larsen, F. Linde, H. Menck, and B. Olsen, "Femoral shaft fracture after hip arthroplasty," *Acta Orthop.*, 1988 Feb; 59(1): 9-13. [PMID: 3354328]; [DOI: 10.3109/17453678809149334]

38 H. Lindahl, G. Garellick, H. Regnér, P. Herberts, And H. Malchau, "Three Hundred and Twenty-One Periprosthetic Femoral Fractures," *J. Bone Jt. Surgery-American Vol.*, vol. 88, no. 6, pp. 1215-1222, 2006,]; [DOI: 10.2106/00004623-200606000-00007].

39 M. J. Raschke and B. Schliemann, "Periprosthetic fractures," *Chirurg*, 2020 Oct; 91(10): 793. [PMID: 32974784]; [DOI: 10.1007/s00104-020-01269-6]

40 Bassam A. Masri, "Periprosthetic fractures: Evaluation and Treatment," *Clin. Orthop.,* 2004; 420: 80-95, [DOI: 10.1097/01.blo.0000122241.70546.eb].

41 R. C. Meinberg E, Agel J, *Fracture and Dislocation Classification Compendium-2018*, vol. 32. 2018.